3D TRUE-AMPLITUDE ANISOTROPIC ELASTIC GAUSSIAN BEAM DEPTH MIGRATION OF 3D IRREGULAR DATA

M.I. PROTASOV [1], V.A. TCHEVERDA[1] and A.P. PRAVDUHIN [2]

[1] Institute of Petroleum Geology and Geophysics,3 Koptyug Street, Novosibirsk 630090,
Russia. protasovmi@ipgg.sbras.ru; cheverdava@ipgg.sbras.ru
[2] INGEOSERVICE, Respubliki Street, Bldg. 211, Tyumen 625019, Russia.
apravduh@ingeos.info

(Received July 10, 2018, revised version accepted January 12, 2019)

ABSTRACT

Protasov, M.I., Tcheverda, V.A. and Pravduhin, A.P., 2019. 3D true-amplitude anisotropic elastic Gaussian beam depth migration of 3D irregular data. *Journal of Seismic Exploration*, 28: 121-146.

True amplitude seismic migration is the procedure, which provides not only the localization of geological objects but also the restoration of their so-called "reflectivity". This characteristic gives very important quantitative additional information about elastic parameters of the objects of interest. The paper addresses 3D seismic depth true-amplitude migration of 3D irregular data in anisotropic media based on beam decomposition of the data. The main objective is the development of the imaging procedure suitable for anisotropic media and handling 3D irregular seismic data without any preliminary regularization. The key components providing the desired image are elastic anisotropic Gaussian beams. Depending on the choice of the beam (quasi P or quasi S) we have PP- or PS-images. Results of synthetic and real data processing are presented and discussed.

KEY WORDS: 3D imaging, Gaussian beams, anisotropy,
irregular multicomponent data.

0963-0651/19/$5.00

INTRODUCTION

Gaussian beams are waves, which are concentrated within the exponentially vanishing vicinity of a ray and are globally regular, that they do never degenerate at singular points of ray fields, like caustic and foci (Nomofilov, 1981; Popov, 2002; Novack, 2012). They form some kind of a full base that is any solution of elastic wave equation can be represented as a superposition of these beams (Babich and Popov, 1989). Hill was the first who use this property of Gaussian beams to write down Green's function in the Kirchhoff integral (Hill, 1990, 2001) and introduce Gaussian beam migration.

The prestack migration procedure presented in (Hill, 2001) operates on common-offset gathers and is extremely efficient because the computation of superposition of very narrow beams isolates summations that do not depend on seismic data and opens a possibility of estimating the result by the asymptotic method of a saddle point. The paper (Gray, 2005) develops Gaussian beam based migration to common-shot records, which handles multi-pathing in a natural way.

Along with the correct recovery of the spatial position of geological objects, it is extremely important to construct their true-amplitude images. As true-amplitude, we have in mind images, which amplitudes are proportional to the so-called reflectivity representing variations of some physical parameters, normally impedance or some of its derivatives. The amplitudes of the imaged events, however, are usually interpreted less precisely. We believe the first Gaussian beam version of true-amplitude pre-stack depth migration was proposed and implemented in (Albertin, 2004). Also in the paper (Gray and Bleistein, 2009) was proposed true-amplitude beam imaging of seismic data in a source-receiver domain. All of the mentioned beam migrations use the wave-field decomposition into Gaussian beams.

In the papers (Protasov and Tcheverda, 2011) proposes another strategy for Gaussian beams based true amplitude pre-stack migration:

1) Individual Gaussian beams are used instead of wave-field decomposition into Gaussian beams;
2) Gaussian beams are traced from the imaging point;
3) The traces of these beams at sources and receivers positions are used as corresponding weights for prestack data summation;
4) Gaussian beams have an equal width at all imaging point;
5) Imaging condition is implemented in terms of structural angles.

This technique provides an asymptotically correct true-amplitude image in acoustic media. The papers (Protasov and Tcheverda, 2012) and (Protasov, 2015) extend this approach to 2D elastic pre-stack migration for multicomponent walkaway Vertical Seismic Profiling (VSP) data and 2D depth migration of multi-component surface seismic data in anisotropic media.

Below we developed this approach for 3D anisotropic media. We created three slightly different 3D beam imaging algorithms. First one is the straightforward generalization of the 2D analog where imaging condition is got in terms of structural angles, Gaussian beams are traced from the image point and they are chosen equal at all image points. This procedure is supposed to be used as a target oriented imaging where a high signal to noise ratio and spatial resolution are achieved. The other two algorithms are the slight modifications where imaging condition is got in terms of acquisition coordinates, and beams are traced from the acquisition and for the last modification beams widths are supposed to be equal at the acquisition system. This way provides a good signal to noise ratio still but faster realizations for big 3D models and for huge 3D seismic data. All algorithms provide the 3D true-amplitude image of 3D/3C seismic data. The proposed approach does not require regularization and can be applied to irregular data either in source-receiver or midpoint-offset domains. P- and S-wave beams can be used to handle raw multi-component data without separating the waves.

BEAM IMAGING METHOD IN 3D

Statement of the true-amplitude imaging problem

Let us consider a 3D heterogeneous anisotropic elastic medium with Lamé's parameters and density decomposing as follows:

$$c_{ijkl} = c_{ijkl}^{0} + c_{ijkl}^{1}, \rho = \rho_0 + \rho_1. \tag{1}$$

The parameters $c_{ijkl}^{0}(x,y,z)$ and $\rho_0(x,y,z)$ describe *a priori* known smooth macro-velocity model/background/propagator, while $c_{ijkl}^{1}(x,y,z)$and $\rho_1(x,y,z)$ are responsible for its rough/rapid perturbations or reflectors.

We introduce a distorted Born approximation (Devaney, 1984) for the reflected/scattered wavefield on the surface:

$$\vec{u}^{obs}(x_r, y_r; x_s, y_s; \omega) =$$
$$= \iint_{R_3^+} G(x_r, y_r, z(x_r, y_r); \xi, \eta, \zeta; \omega) \cdot L_1 < \vec{u}_0(\xi, \eta, \zeta; x_s, y_s, z(x_s, y_s); \omega) > d\xi d\eta$$
$$x_r^1 \le x_r \le x_r^2; y_r^1 \le y_r \le y_r^2; \quad x_s^1 \le x_s \le x_s^2; y_s^1 \le y_s \le y_s^2; \quad \omega_1 \le \omega \le \omega_2. \tag{2}$$

Here $(x_r, y_r, z(x_r, y_r))$ is the receiver coordinate, $(x_s, y_s, z(x_s, y_s))$ is the source coordinate, ω is the frequency and $\vec{u}_0$ is the incident wavefield propagating in a smooth background from a volumetric point source with impulse $F(\omega)$, $G(x_r, 0; \xi, \eta; \omega)$ - Green's matrix for the smooth background and operator L_1 introducing by the rough perturbations $c_{ijkl}^1(x, y, z)$ and ρ_1:

$$(L_1 < \vec{u}_0 >)_{x_j} \equiv -\sum_{i,l,k=1}^{3} \frac{\partial}{\partial x_i}\left(c^1{}_{ijkl} \frac{\partial u_{0x_l}}{\partial x_k} \right) - \rho_1 \omega^2 u_{0x_j}; \; x_1 \equiv x, x_2 \equiv y, x_3 \equiv z. \tag{3}$$

The problem is to reconstruct rough perturbations of elastic parameters c_{ijkl}^1 and density ρ_1 or some of their combinations by resolving integral eq. (3) with the data $\vec{u}^{obs}(x_r, y_r; x_s, y_s; \omega)$.

Target oriented imaging condition: structural angles and equal beams at the image point

From every imaging point $\bar{x} = (x_i, y_i, z_i)$, we trace a pair of quasi-pressure (qP) rays. One of them is traced to the receiver positions, another - towards the source positions. These rays are completely defined by the macro-model parameters $c_{ijkl}^0(x_1, x_2, x_3)$, $\rho(x_1, x_2, x_3)$ and by the structural angles γ, θ and az, β_1, β_2 (see Fig. 1). Angles γ, θ define a structural vector $\vec{n} = (\cos\theta \cdot \sin\gamma, \sin\theta \cdot \sin\gamma, \cos\gamma)$, i.e., structural dip γ and structural azimuth θ. Angle az defines the plane of ray propagation at the image point, i.e., azimuth of rays incidence. Angles β_1, β_2 are opening angles and for isotropic media they are equal, but for the anisotropic case they are different and they are connected by the Snell's law for anisotropic media:

$$\frac{\sin(\beta_2)}{c_{qp}(\bar{x};az,\beta_2)} = \frac{\sin(\beta_1)}{c_{qp}(\bar{x};az,\beta_1)}$$

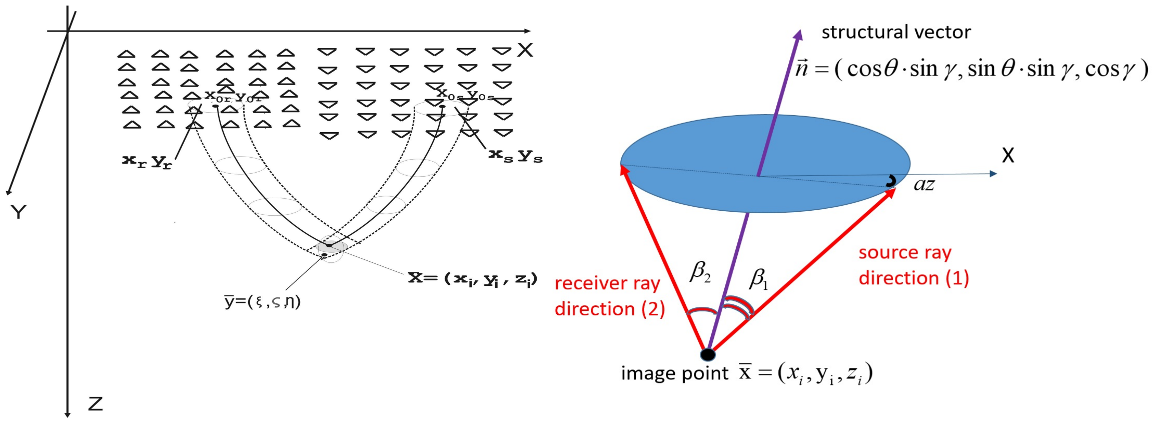

(a) (b)

Fig. 1. (a) The geometry of the method. (b) Structural angles.

Because opening angles β_1, β_2 depend on each other we write below the dependence with respect to β_2 only. We define the receiver ray by the index «1», and source ray by the index «2» and construct qP Gaussian beams concentrated these rays (Nomofilov, 1981) and denote them as $\vec{u}_{qp}^{gb1}(x_r, y_r;\bar{x};\gamma,\theta,az,\beta_2;\omega)$, $\vec{u}_{qp}^{gb2}(x_s, y_s;\bar{x};\gamma,\theta,az,\beta_2;\omega)$. Then on the acquisition, we compute two summation weights: one is the normal derivative of the Gaussian beam in the receivers area, another one is the normal derivative of the scalar part of the corresponding beam in the source area:

$$\vec{T}_{qp}^{gb1}(x_r, y_r;\bar{x};\gamma,\theta,az,\beta_2;\omega), T_{qp}^{gb2}(x_s, y_s;\bar{x};\gamma,\theta,az,\beta_2;\omega). \tag{4}$$

The initial width for both Gaussian beams is fixed at the image point. Therefore, one can control the beam's width by using the dimensionless parameter (for example, number of wavelengths) and, consequently, one can control the image resolution. The smallest possible beam width at the image point should yield the best image resolution (sharp imaging kernel).

We multiply both parts of the "single scattering" integral (2) by the constructed weights (4) and integrate with respect to the source and receiver coordinates. Using saddle point technique for every beam weight (it is the straightforward 3D analog of the result described in the paper (Protasov, 2015)), we come to the following identity:

$$\int_{R^3} \vec{u}_{qp}^{gb1}(\xi,\eta,\zeta;\bar{x};\gamma,\theta,az,\beta_2;\omega)\cdot L_1\left\langle \vec{u}_{qp}^{gb2}(\xi,\eta,\zeta;\bar{x};\gamma,\theta,az,\beta_2;\omega)\right\rangle d\zeta d\eta d\xi =$$
$$= \int T_{qp}^{gb2}(x_s,y_s;\bar{x};\gamma,\theta,az,\beta_2;\omega)\vec{T}_{qp}^{gb1}(x_r,y_r;\bar{x};\gamma,\theta,az,\beta_2;\omega)\cdot\vec{\varphi}(x_r,y_r;x_s,y_s;\omega)dx_r dy_r dx_s dy_s. \tag{5}$$

Then, we use the following representation of qP beams:

$$\vec{u}_{qp}^{gb1,2} = \vec{e}_{qp}^{\,1,2}\varphi_{qp}^{gb1,2},$$

and compute beam derivatives (operator L_1) retaining terms up to the first order only, The microlocal analysis (it is analogous to the analysis described in the paper by (Protasov and Tcheverda, 2011)) of the left-hand side of (5) gives the following:

$$\omega^2\int_{R^3}\exp(i\omega(\nabla\tau^{(1)}(\bar{\mathrm{x}};\gamma,\theta,\beta_1)+\nabla\tau^{(2)}(\bar{\mathrm{x}};\gamma,\theta,\beta_2))\cdot(\xi-x_i,\eta-y_i,\zeta-z_i))\cdot f^{qpqp}(\xi,\eta,\zeta)d\zeta d\eta d\xi =$$
$$\int T_{qp}^{gb2}(x_s,y_s;\bar{x};\gamma,\theta,az,\beta_2;\omega)\vec{T}_{qp}^{gb1}(x_r,y_r;\bar{x};\gamma,\theta,az,\beta_2;\omega)\cdot\vec{\varphi}(x_r,y_r;x_s,y_s;\omega)dx_r dy_r dx_s dy_s. \tag{6}$$

Now let us change variables $(\gamma,\theta,\omega)\rightarrow(p_x,p_y,p_z)$ by the implicit function:

$$\vec{p} = \omega(\nabla\tau^1(\xi,\eta,\zeta;\gamma,\theta,az,\beta_2)+\nabla\tau^2(\xi,\eta,\zeta;\gamma,\theta,az,\beta_2)), \tag{7}$$

After multiplication of (6) by

$$k(\bar{x};\gamma,\theta,az,\beta_2) = \left(\frac{\cos(\beta_2)}{c_{qp}(\bar{x};az,\beta_2)}+\frac{\cos(\beta_1)}{c_{qp}(\bar{x};az,\beta_1)}\right)^3\cos(\theta)$$

and integration with respect to γ,θ,ω, we come to the imaging condition with respect to structural angles:

$$M < f^{qpqp} > (\bar{x}) = \int T_{qp}^{gb2}(x_s,y_s;\bar{x};\gamma,\theta,az,\beta_2;\omega)\vec{T}_{qp}^{gb1}(x_r,y_r;\bar{x};\gamma,\theta,az,\beta_2;\omega)\cdot$$
$$\cdot\vec{\varphi}(x_r,y_r;x_s,y_s;\omega)k(\bar{x};\gamma,\theta,az,\beta_2)dx_r dy_r dx_s dy_s d\omega d\gamma d\theta. \tag{8}$$

The operator M is the almost identity operator and is represented as the superposition of the Fourier transform of the scattering potential:

$$f^{qpqp} = \sum_{i,j,l,k=1}^{2} c^{1}{}_{ijkl} \cdot g_j^2 \cdot g_l^1 \cdot p_i^2 \cdot p_k^1 + \rho^1 \cdot g_j^2 \cdot g_l^1 \qquad (9)$$

and its quasi-inverse. It is not an exact inverse Fourier transform because integration is performed not over the whole phase space but over its subdomain later referred to as the domain of *partial reconstruction*. In particular, if a support of the Fourier image of a function does not belong to this domain, this function is from the kernel of this "almost identity" operator.

The procedure is naturally multi-component. Any Gaussian beam for elastic media has qP- or qS-wave polarization. The imaging condition includes the scalar product of the beam polarization vector and polarization vector of the recorded wave field. In particular, this product of unit polarization vectors of Gaussian qP-beam and upgoing qP-wave gives almost one, but for Gaussian qP-beam and upgoing qS-wave is almost zero. Therefore on a PP image, there are no artifacts produced by the PS waves.

Ray tracing from the image point controls structural angles ($\gamma, \theta, az, \beta_2$), therefore, integrals in the realization of the imaging condition (8) with respect to structural angles can be computed easily, hence the true amplitude selective images (which are images for the fixed structural angels) are computed easily as well. It is worth mentioning that these kind of images, so-called selective images, are extremely important for the detection of diffractions produced by subseismic objects (Protasov et al., 2016). However, in such an algorithm for every image point and for every value of structural angles one should compute the corresponding weights and also one should find and load the corresponding part of the seismic data. In this case, the computational time is rather big for any serious 3D seismic acquisition, where data space, as a rule, is much larger than a hundred gigabytes. But because the computational time depends on the number of image points and structural angles then it can be reasonable for the small image area. Therefore, the described algorithm can serve as target-oriented high-resolution imaging approach.

Imaging condition: acquisition coordinates

Instead of structural angles $\gamma, \theta, az, \beta_2$ the alternative parametrization of the rays is offset and common middle point $x_{m0}, y_{m0}, h_{x0}, h_{y0}$, which are defined by the ray coordinates on the acquisition surface as follows:

$$x_{m0} = \frac{x_{r0} + x_{s0}}{2}, y_{m0} = \frac{y_{r0} + y_{s0}}{2}, h_{x0} = x_{r0} - x_{s0}, h_{y0} = y_{r0} - y_{s0}.$$

Then we can use parametrization $x_{m0}, y_{m0}, h_{x0}, h_{y0}$ in (6) do the change of variables $(x_{m0}, y_{m0}, \omega) \to (p_x, p_y, p_z)$ in the following manner:

$$\vec{p} = \omega(\nabla\tau^1(\xi,\eta,\zeta;\mathrm{x}_{\mathrm{m0}},\mathrm{y}_{\mathrm{m0}},h_{x0},h_{y0}) + \nabla\tau^2(\xi,\eta,\zeta;\mathrm{x}_{\mathrm{m0}},\mathrm{y}_{\mathrm{m0}},h_{x0},h_{y0})).$$

Now let us multiply both parts of (6) by the Beylkin's determinant (Beylkin, 1985)

$$BelDet = \begin{vmatrix} \nabla(\tau^1+\tau^2)_x; & \nabla(\tau^1+\tau^2)_y; & \nabla(\tau^1+\tau^2)_z \\ \dfrac{\partial\nabla(\tau^1+\tau^2)_x}{\partial x_{m0}}; & \dfrac{\partial\nabla(\tau^1+\tau^2)_y}{\partial x_{m0}}; & \dfrac{\partial\nabla(\tau^1+\tau^2)_z}{\partial x_{m0}} \\ \dfrac{\partial\nabla(\tau^1+\tau^2)_x}{\partial y_{m0}}; & \dfrac{\partial\nabla(\tau^1+\tau^2)_y}{\partial y_{m0}}; & \dfrac{\partial\nabla(\tau^1+\tau^2)_z}{\partial y_{m0}} \end{vmatrix},$$

and integrate with respect to x_{m0}, y_{m0}, ω.

Finally, we come to the imaging condition in terms of the common midpoint, offset:

$$M < f^{qpqp} > (\bar{x}) = \int \vec{T}^{gb1}_{qp}\left(x_r, y_r; \bar{x}; \mathrm{x}_{\mathrm{m0}}, \mathrm{y}_{\mathrm{m0}}, h_{x0}, h_{y0}; \omega\right) \cdot \vec{\varphi}\left(x_r, y_r; x_s, y_s; \omega\right) \times$$
$$\times T^{gb2}_{qp}\left(x_s, y_s; \bar{x}; \mathrm{x}_{\mathrm{m0}}, \mathrm{y}_{\mathrm{m0}}, h_{x0}, h_{y0}; \omega\right) \cdot BelDet \cdot dx_r dy_r dx_s d\mathrm{y}_s d\omega dx_{m0} dy_{m0}. \quad (10)$$

In the common industrial technology of seismic processing, the data are often sorted by common midpoint (x_m, y_m) and offset (h_x, h_y). Therefore on the left-hand side of (10), we need to change variables $(x_r,y_r,x_s,y_s) \rightarrow (x_m,y_m,h_x,h_y)$:

$$I(\bar{x};h_{x0},h_{y0}) = \int \vec{T}_{qp}^{gb1}\left(x_m,y_m,h_x,h_y;\bar{x};x_{m0},y_{m0},h_{x0},h_{y0};\omega\right)\cdot \vec{\varphi}\left(x_m,y_m,h_x,h_y;\omega\right)$$

$$T_{qp}^{gb2}\left(x_m,y_m,h_x,h_y;\bar{x};x_{m0},y_{m0},h_{x0},h_{y0};\omega\right)\cdot BelDet \cdot dx_m dy_m dh_x d\mathrm{h}_y d\omega dx_{m0} dy_{m0}. \tag{11}$$

Now the weights (4) are defined in mid-point\offset coordinates:

$$\vec{\mathrm{T}}_{qp}^{gb1}(x_m,y_m,h_x,h_y;\bar{x};x_{m0},y_{m0},h_{x0},h_{y0};\omega), \quad T_{qp}^{gb2}(x_m,y_m,h_x,h_y;\bar{x};x_{m0},y_{m0},h_{x0},h_{y0};\omega). \tag{12}$$

In this case, ray tracing is done from a fixed set of points on the acquisition surface to all the points of the medium, where an image is built, for that we use approximate anisotropic ray tracing (Dehghan, 2007), and paraxial ray tracing (Gibson, 1991). And then for a fixed offset, we should construct an image (at all the points of the medium) for all central midpoints that define a pair of beam centers in the receivers and sources, respectively. In addition, if we set the migration aperture on the acquisition surface, there will be no need to build an image in the whole region and there will be no need to solve the direct problem in the whole region but within the aperture only.

This approach provides technological workflow of the migration procedure. First of all, attributes are computed apart from the summation procedure. Also, attributes are computed for the predefined sparse grid of beam centers and they are computed on the sparse image grid within the migration aperture. Such way allows computing attributes for rather huge models within the reasonable computational time. In the summation procedure for every source-receiver pair of beam centers the data are loaded once and then their summation is done for all image points within the migration apertures. In comparison with the version where shooting is done from the image, there is no necessity to find the data for each image point. Finally, in such case, the migration is much faster in comparison with shooting from the bottom.

However, even in this case, the most technologically advanced procedure of summation depends on the Gaussian beams. In the case when the width of the Gaussian beams is controlled in the image points the summation of uploaded data for each pair is done with different weights for different image points. Therefore the computational time of summation procedure is rather huge for big 3D seismic acquisition. However, in this case, the image quality is got with the best resolution.

Imaging condition: equal beams at the acquisition system

The other option is to control beam width at the acquisition surface, more precisely, we provide equal beams width for each beam center. First of all, we can integrate the left-hand side of (11) with respect to ω explicitly:

$$I(\bar{x};h_{x0},h_{y0}) = \int \vec{T}_{qp}^{gb1}\left(x_m,y_m,h_x,h_y;\bar{x};x_{m0},y_{m0},h_{x0},h_{y0}\right)\cdot \vec{\varphi}\left(x_m,y_m,h_x,h_y;t=\tau_1+\tau_2\right)$$
$$T_{qp}^{gb2}\left(x_m,y_m,h_x,h_y;\bar{x};x_{m0},y_{m0},h_{x0},h_{y0}\right)\cdot BelDet\cdot dx_m dy_m dh_x dh_y dx_{m0} dy_{m0}. \tag{13}$$

Let us rewrite the product of weights and Beylkin determinant in the following form:

$$\begin{aligned}&\vec{T}_{qp}^{gb1}\left(\mathrm{x}_{\mathrm{m}},y_m,\mathrm{h}_{\mathrm{x}},h_y;\bar{x};\mathrm{x}_{\mathrm{m0}},\mathrm{y}_{\mathrm{m0}},h_{x0},h_{y0}\right)\cdot T_{qp}^{gb2}\left(\mathrm{x}_{\mathrm{m}},y_m,\mathrm{h}_{\mathrm{x}},h_y;\bar{x};\mathrm{x}_{\mathrm{m0}},\mathrm{y}_{\mathrm{m0}},h_{x0},h_{y0}\right)\cdot BelDet = \\ &= \vec{A}(\bar{x};\mathrm{x}_{\mathrm{m0}},\mathrm{y}_{\mathrm{m0}},h_{x0},h_{y0})\cdot T_{gb}^{m}(\mathrm{x}_{\mathrm{m1}},y_{m1})\cdot T_{gb}^{h}(h_{\mathrm{x1}},h_{y1}).\end{aligned} \tag{14}$$

Here $x_{m1} = x_m - x_{m0}, y_{m1} = y_m - y_{m0}, \cdot h_{\mathrm{x1}} = h_{\mathrm{x}} - h_{\mathrm{x0}}, h_{y1} = h_y - h_{y0}$. Then imaging condition (13) takes the form:

$$\begin{aligned}&I(\bar{x};h_{x0},h_{y0}) = \int \vec{A}(\bar{x};x_{m0},y_{m0},h_{x0},h_{y0})\cdot T_{gb}^{m}(x_{m1},y_{m1})\cdot T_{gb}^{h}(h_{x1},h_{y1})\cdot \\ &\vec{\varphi}\left(x_m,y_m,h_x,h_y;t=\tau_1+\tau_2\right)dx_{m1}dy_{m1}dh_{x1}dh_{y1}dx_{m0}dy_{m0}\end{aligned} \tag{15}$$

We have to note beam travel times τ_1,τ_2 consist of travel times between beam center points and image point $\tau_{12}^0 = \tau_1^0 + \tau_2^0$ and beam travel time shift according to the source-receiver shift from beam centers:

$$\tau_1 + \tau_2 = \tau_{12}^0(\bar{x};x_{m0},y_{m0},h_{x0},h_{y0}) + p_{mx0}\cdot x_{m1} + p_{my0}\cdot y_{m1} + p_{hx0}\cdot h_{x1} + p_{hy0}\cdot h_{y1}. \tag{16}$$

As one can conclude, the summation procedure can be split into two stages:

1) the decomposition of the data into beams

$$\vec{D}_{gb}(x_{m0},y_{m0};h_{x0},h_{y0};t;p_{mx0},p_{my0};p_{hx0},p_{hy0}) =$$
$$= \int \vec{\varphi}\left(x_m,y_m,h_x,h_y;t + p_{mx0}\cdot x_{m1} + p_{my0}\cdot y_{m1} + p_{hx0}\cdot h_{x1} + p_{hy0}\cdot h_{y1}\right)\cdot \quad (17)$$
$$T^{m}_{gb}(x_{m1},y_{m1})\cdot T^{h}_{gb}(h_{x1},h_{y1})dx_{m1}dy_{m1}dh_{x1}dh_{y1};$$

2) the mapping procedure:

$$I(\bar{x};h_{x0},h_{y0}) = \int \vec{D}_{gb}(x_{m0},y_{m0};h_{x0},h_{y0};t = \tau^{0}_{12};p_{mx0},p_{my0};p_{hx0},p_{hy0})\cdot$$
$$\cdot\vec{A}(\bar{x},x_{m0},y_{m0},h_{x0},h_{y0})dx_{m0}dy_{m0}.$$
$$(18)$$

Finally, we have got the procedure consisting of data decomposition and mapping of decomposed data to the image domain. This way leads to the rather fast parallel beam imaging software and, hence, opens the possibility to migrate huge seismic data up to terabytes within the reasonable computational time.

Below we provide some comparison of the imaging condition (17)-(18). If we assume that the weight is computed in the offset domain $T^{h}_{gb}(h_{x1},h_{y1}) = \delta(h_{x1},h_{y1})$, then we come to the multi-component, anisotropic true-amplitude analog of the beam migration proposed by Hill (2001). In this case, the beam decomposition of the data is done only in mid-point domain:

$$\vec{D}_{gb}(x_{m0},y_{m0};h_x,h_y;t;p_{mx0},p_{my0}) =$$
$$= \int \vec{\varphi}\left(x_m,y_m,h_x,h_y;t + p_{mx0}\cdot x_{m1} + p_{my0}\cdot y_{m1}\right)\cdot T^{m}_{gb}(x_{m1},y_{m1})\cdot dx_{m1}dy_{m1}; \quad (19)$$

followed by the mapping procedure for each offset:

$$I(\bar{x};h_x,h_y) = \int \vec{D}_{gb}(x_{m0},y_{m0};h_x,h_y;t = \tau^{0}_{12};p_{mx0},p_{my0})\cdot$$
$$\vec{A}(\bar{x},x_{m0},y_{m0},h_x,h_y)dx_{m0}dy_{m0} \quad (20)$$

By comparison of (19) and (20) with the full decomposition (17) and (18) we may conclude that the computational cost can be similar (it depends on the number of offsets that we really need to compute in (18)), but for the last variant the data must be regular in common midpoint offset domain, however, the data can be irregular for the first case. Also in this case beam decomposition with respect to offsets is performed which gives additional image quality profit. We have to underline that almost all real data geometries provide irregular data, especially land acquisitions.

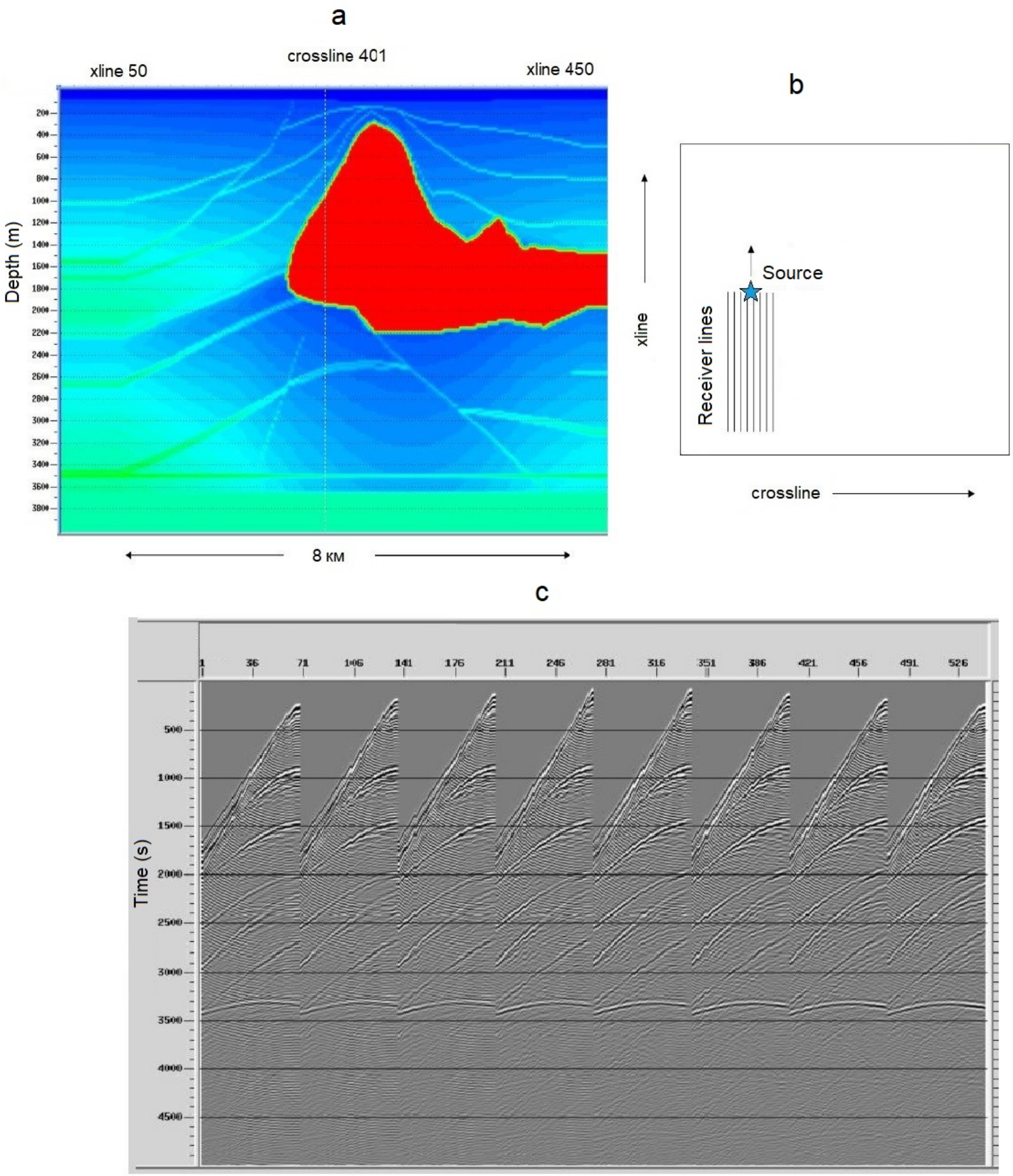

Fig. 2. Two-dimensional section of the three-dimensional model SEG-salt - (a); an acquisition system simulating marine seismic survey - (b); synthetic data for one source based on the results of finite-difference modeling - (c).

RESULTS OF DATA PROCESSING

Synthetic data sets processing

All numerical examples are presented for the algorithms where beams are traced from the acquisition system i.e. realizations of imaging condition (11) and imaging condition (18) where full beam decomposition is proposed. To verify the approach and software developed we use one of the most well-known 3D data sets, it is the freely available data for the SEG-salt model [SEG / EAGE 3D modeling Salt Model Phase-C, 1996]. The model is three-dimensional and contains a salt body (Fig. 2a). The dataset simulates marine seismic survey, in which observations consist of 51 lines of the ship's motion, the distance between which is 320 m. On each line 96 sources, the interval between sources along the line is 80 m (Fig.2b). The signal from each source (Fig. 2c) is fixed by 8 cables, the distance between them is 40 m, with each receiver accounting for 68 receivers with a distance of 20 m between them.

For this model and the data, two tests of the migration are carried out. One of them is implemented for the smoothed SEG-salt model through Kirchhoff industrial migration. In this case, the smoothing of the model is selected in such a way as to obtain the best quality image of the lower horizontal interface at a depth of about 3500 meters. Comparison of the two-dimensional sections of the SEG-salt model (Figs. 3c, 4c) and similar sections of the three-dimensional image from the Kirchhoff migration (Figs. 3e, 4e) show that the position of this interface is restored in many places quite well. The same results demonstrate a fairly good recovery of the lower boundary of the salt body, but at the same time with this, the upper interface of Kirchhoff migration result is rather blurred and defocused. Another test was done using developed Gaussian beam migration, also here a special tracing algorithm for a more correct description of the rays through the salt body. Comparison of the two-dimensional sections of the SEG-salt model (Figs. 3c, 4c) and similar sections of the three-dimensional image from the Kirchhoff migration (Figs. 3e, 4e), as well as the slices from the Gaussian beam migration result (Figs. 3a, 4a) show that the lower horizontal interface at a depth of 3500 meters much better restored using Gaussian beam migration than Kirchhoff migration with the "optimal" smoothing of the model. It is also obvious that in the subsalt zone at a depth between 2000 and 3000 meters the dipping reflector is restored quite confidently in the Gaussian beam migration image, whereas on the Kirchhoff migration it is almost absent. Moreover, the salt interface is more reliably determined by the Gaussian beam migration results (Figs. 3b, 4b) than by the Kirchhoff migration results (Figs. 3f, 4f).

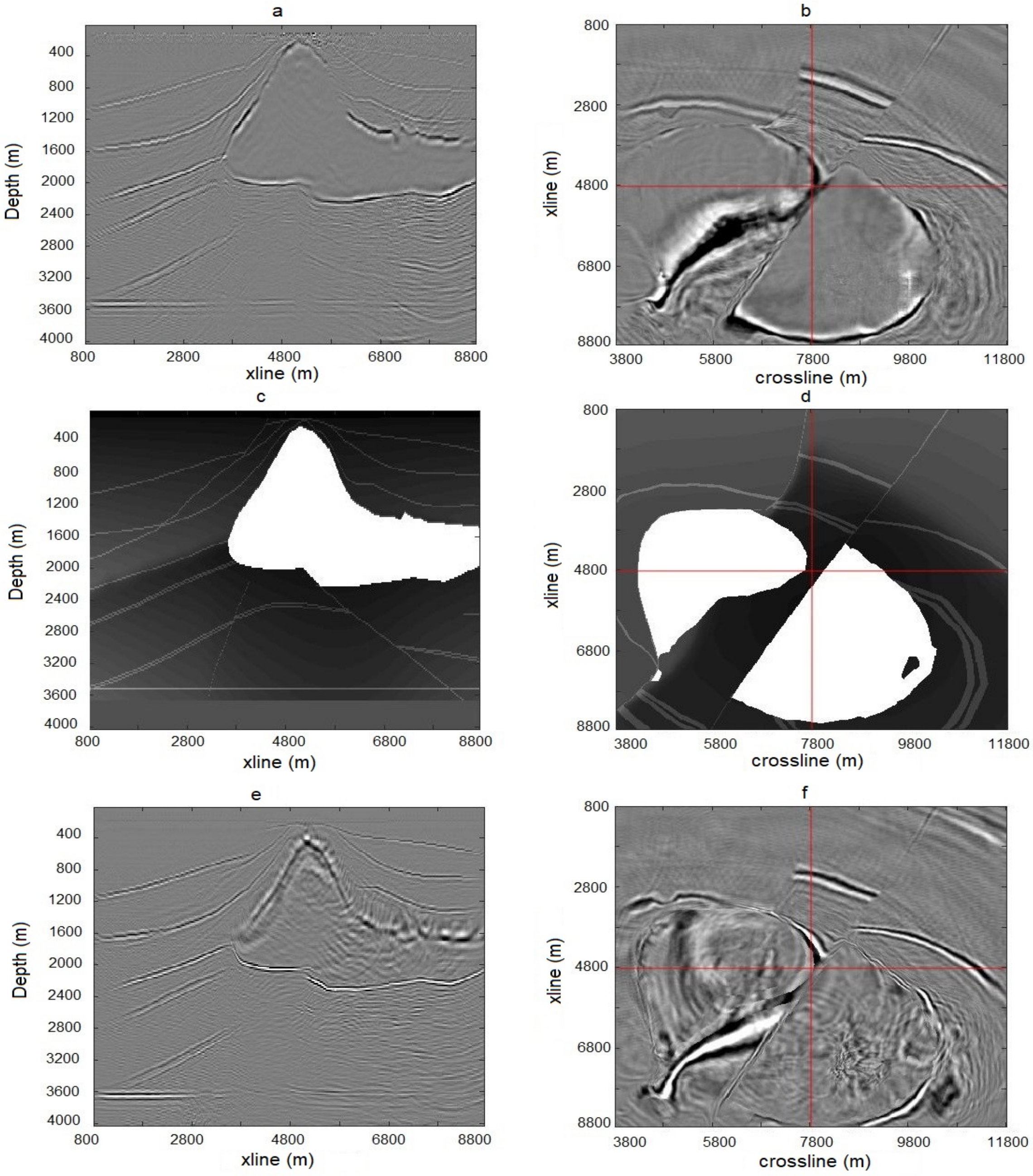

Fig. 3. Two-dimensional sections of the three-dimensional model SEG-salt, with the coordinate crossline = 7800 m - (c), at a depth of 2000 m - (d); two-dimensional sections of a three-dimensional image of Gaussian beam migration, with the coordinate crossline = 7800 m - (a), at a depth of 2000 m - (b); two-dimensional sections of a three-dimensional image of Kirchhoff migration, with a coordinate of crossline = 7800 m - (e), at a depth of 2000 m - (f).

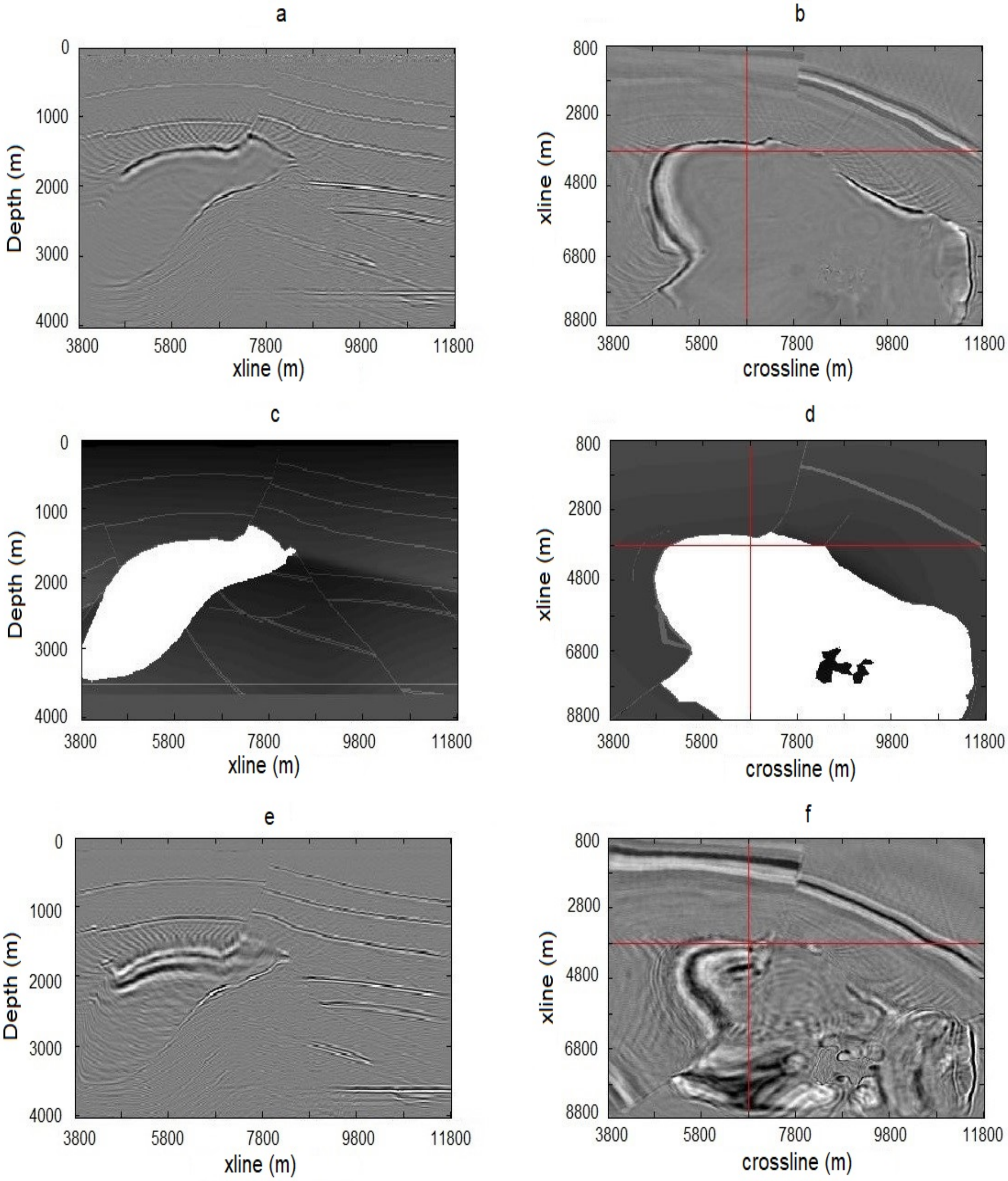

Fig. 4. Two-dimensional sections of the three-dimensional model SEG-salt, with the coordinate xline = 3800 m - (c), at a depth of 3000 m - (d); two-dimensional sections of a three-dimensional image of Gaussian beam migration, at a coordinate xline = 3800 m - (a), at a depth of 3000 m - (b); two-dimensional sections of a three-dimensional image of Kirchhoff migration, at a coordinate xline = 3800 m - (e), at a depth of 3000 m - (f).

Real data depth imaging

Next, the developed Gaussian beam migration algorithm has been tested on the real data. First, it was applied to the 2D land data from Western Siberia. Several common midpoint gathers are presented on the Fig. 5a. The depth migration model was got by anisotropic common image point tomography. P-velocity and Thomsen parameters are presented in Fig. 5. One can observe maximum parameters values provide 20% of anisotropy. For these model and data, both beam imaging algorithms were applied ,i.e., realizations of imaging condition (11) and imaging condition (18). The imaging results of both approaches are very similar in this case because the quality of data is rather good and the model is rather simple. Therefore we provide the imaging results of the algorithm that is realizations of the imaging condition (11) in comparison with the Kirchhoff migration results got by the commercial processing system. The image stack produced by Kirchhoff migration is shown in Fig. 6a and the image stack obtained by Gaussian beam migration is presented in Fig. 6b. The corresponding common image gathers (CIGs) calculated by a Kirchhoff migration can be seen in Fig. 11a and CIGs computed by the beam imaging can be found in Fig. 7b. The beam migration algorithm produces CIGs and a full stacked image that are much cleaner and less noisy than Kirchhoff migration results.

Then we have got the results for 3D surface seismic real data and 3D acquisition from the Kara Sea. These are the marine seismic data where towed streamers (12 pieces) are used: 6000 meters long, the distance between streamers is 100 meters, the distance between receivers is 12.5 meters, i.e., 480 receivers per braid. The interval between the sources is 25 m, the spacing between the source lines is 600 m, the distance from the source to the nearest receiver varies between 175-185 m. The maximum offset in the data is 6000 m, and their fold is 240. Before processing the data, the binning in common midpoint (CMP) domain was applied with bins sizes 12.5 m by 25 m. An example of several CMP (common midpoint) gathers is presented in Fig. 8. Though trace coordinates in CMP domain are regular (see Figs. 9a, 9b) the traces coordinates in vector offset domain are irregular (see Figs. 9c, 9d, 9e). Therefore, for the “standard” beam migration one needs to provide data regularization in the vector-offset domain. However, the developed beam procedures allow computing images in any point within the acquisition limits. So the image can be computed on rather irregular and rather dense or sparse acquisition grid.

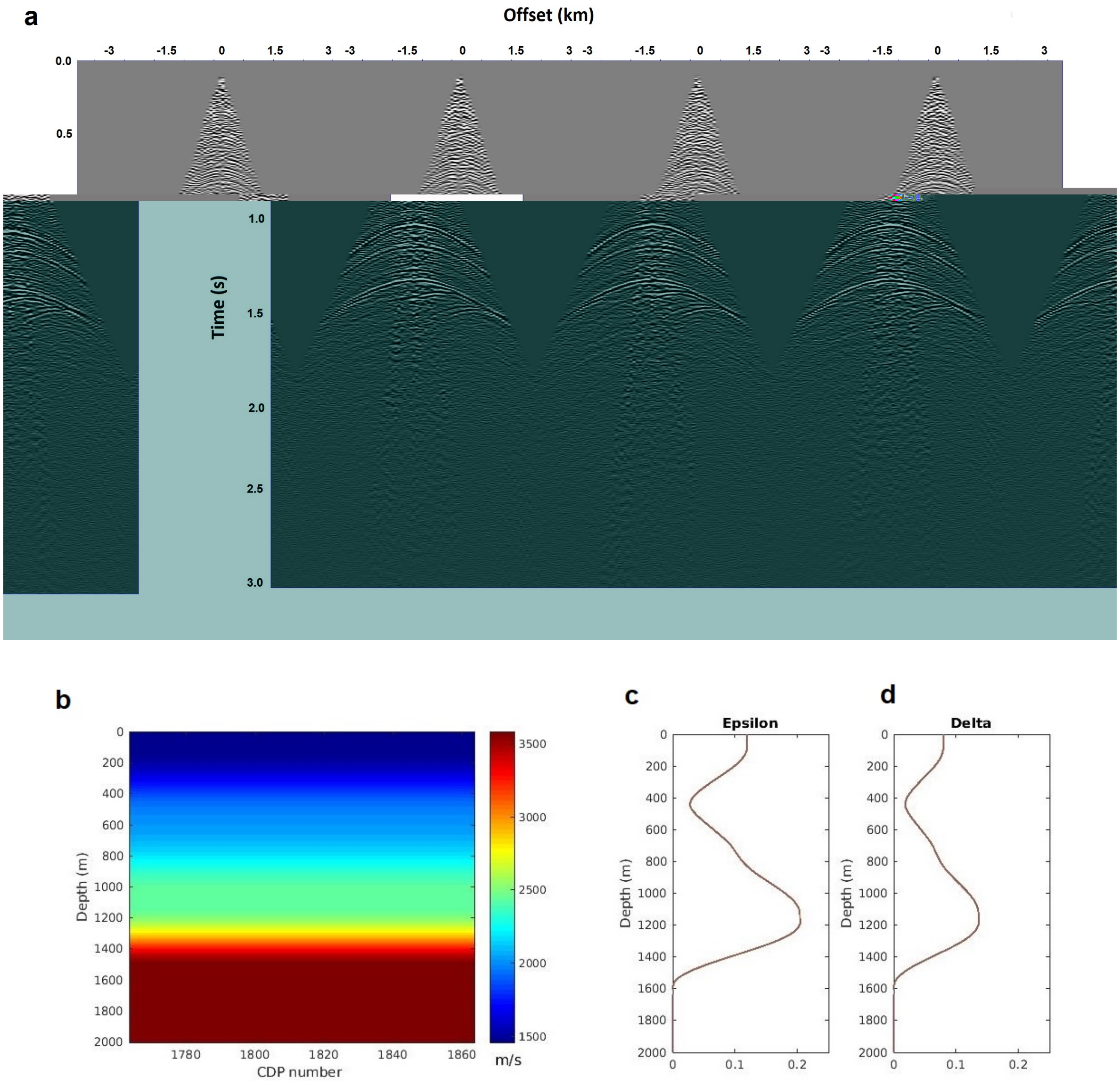

Fig. 5. (a) Several common mid-point gathers of 2D seismic data from Western Siberia; migration velocity model. (b) P-velocity. (c) Thomsen parameter ε .
(d) Thomsen parameter δ .

These data went through the full processing workflow. First time processing and then depth processing. At the last stage, pre-stack depth migration was performed. Before this stage, a depth velocity model was constructed. For that purpose common image point (CIP) tomography was used. First, the migration process followed by CIP tomography is repeated until CIP gathers provide non-flat events. Next, tying a well to seismic data further tomographic refinement of the model is carried out taking into account a priori information. Well data contain information about the anisotropy of the environment, therefore, after the well information is taken into account, a priori information about the anisotropy is entered into the model and specified in the process of tomographic inversion. Finally, an anisotropic migration model of the environment is constructed. To obtain a satisfactory migration depth velocity model, in this case, 26 iterations of migration and tomography were performed. It is clearly seen that the anisotropic parameters are the functions of both depth and horizontal directions (Fig. 10). The maximum value of the Thomsen parameter δ reaches 0.05, and the maximum value of the Thomsen parameter ε reaches 0.1, where the main anisotropic layers start from the seabed and reach the depth of 1300 m (Fig. 11).

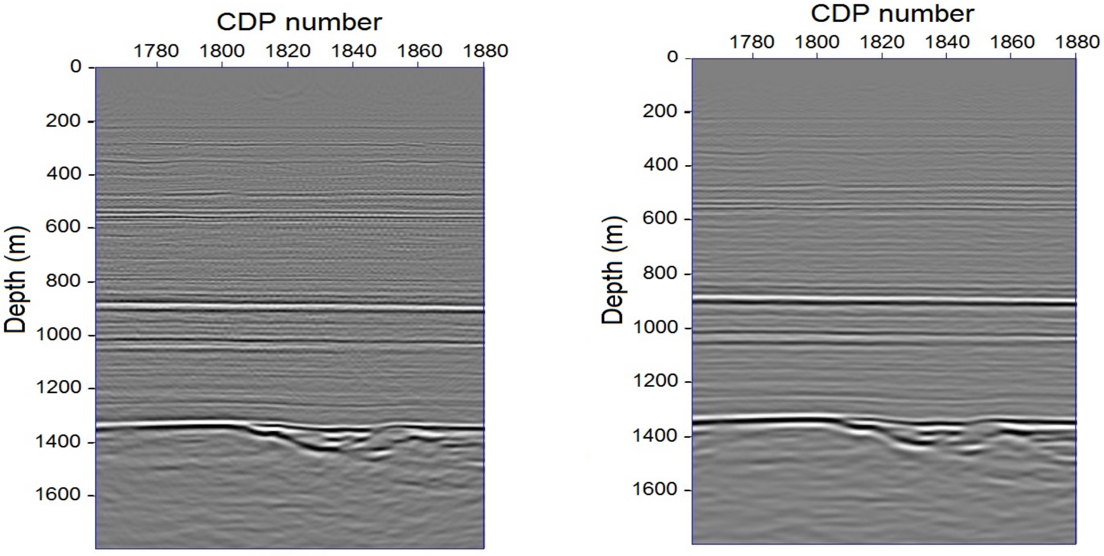

(a) (b)

Fig. 6. (a) Kirchhoff migration: an image stack in the anisotropic model. (b) Beam migration: an image stack in the anisotropic model.

Finally, at the last stage of processing, the developed beam migration algorithm was applied to these 3D real data. The 3D image stack and CIP gathers are presented on the Fig. 12a where all seismic interfaces are traced quite clearly, thanks to the good ratio signal/noise which can be achieved by target oriented massive summation of the data in the beam migration process. On the CIP gathers provided by Gaussian beam migration, seismic events are horizontal. Particularly, it means the anisotropy in the migration process is taken into account correctly (Fig. 12b), the section as a whole is quite resolved, and the seismic events are fairly focused. Fig. 13b represents the image stack obtained by the commercial Kirchhoff migration. Fig. 13a presents the image stack that is got by beam imaging according to eqs. (17) and (18). From a comparison of images obtained in this way, it follows that the resolution of migration on Gaussian beams exceeds the resolution of Kirchhoff's migration, the seismic horizons in the image obtained by Gaussian beams are better traced than in the image obtained by Kirchhoff's migration (Fig. 13). Also, we compared the computational time of the developed beam imaging algorithm and commercial Kirchhoff migration. The image presented on the Fig. 12a were got for the area 300 km^2 and the computational time was about 18 hours. The computational resources contain 10 nodes with 20 cores on each computation node. The computation time of Kirchhoff migration was about 16 hours on the same environment. So computational times are rather similar but the image quality of the beam migration is better.

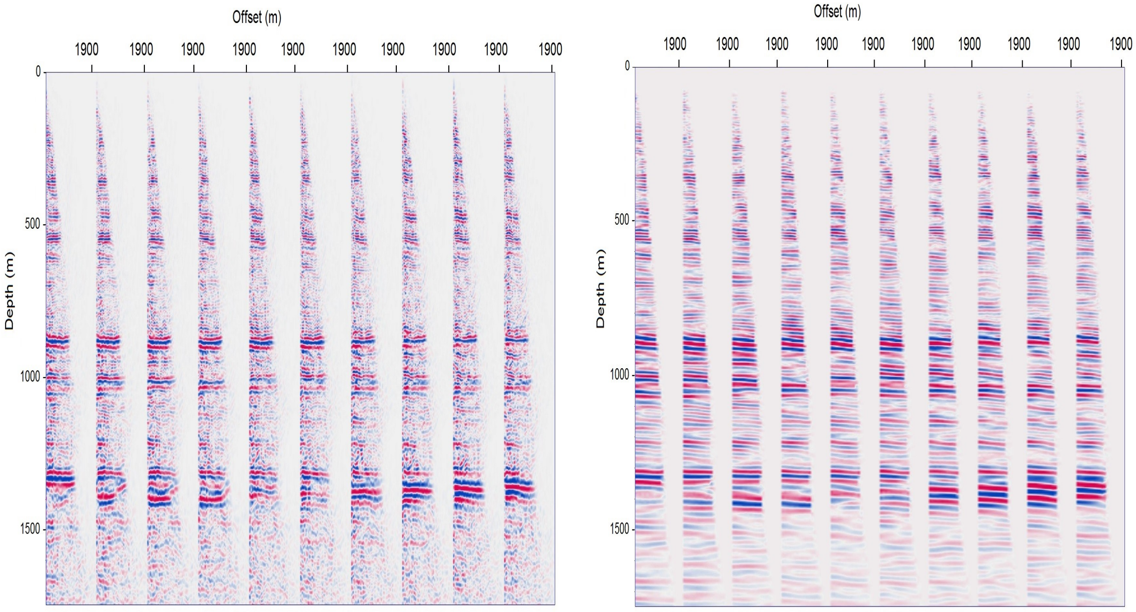

(a) (b)

Fig. 7. a) Kirchhoff migration: CIGs in anisotropic model. b) Beam migration: CIGs in the anisotropic model.

CONCLUSION AND DISCUSSION

We developed three-dimensional anisotropic Gaussian-beam migration algorithms for irregular 3D/3C seismic data. We created three slightly different 3D beam imaging algorithms. Also, all three algorithms use:

1) Individual Gaussian beams instead of wave-field decomposition into Gaussian beams;
2) Traces of the beams as weights for prestack data summation.

The first one is a straightforward generalization of the 2D analog where:

1) Gaussian beams are traced from the *imaging point*;
2) Gaussian beams have an equal width at all *imaging point*;
3) Imaging condition is implemented in terms of *structural angles*.

This procedure is supposed to be used as a target oriented imaging and object-oriented imaging where a high signal to noise ratio and spatial resolution are achieved. So we propose to use this procedure for imaging of small-scale heterogeneity i.e. for diffraction imaging where such properties are extremely important.

The other algorithm is slight modification where:

1) Gaussian beams are traced from the *acquisition points*;
2) Gaussian beams have an equal width at all imaging points;
3) Imaging condition is implemented in terms of *acquisition coordinates*.

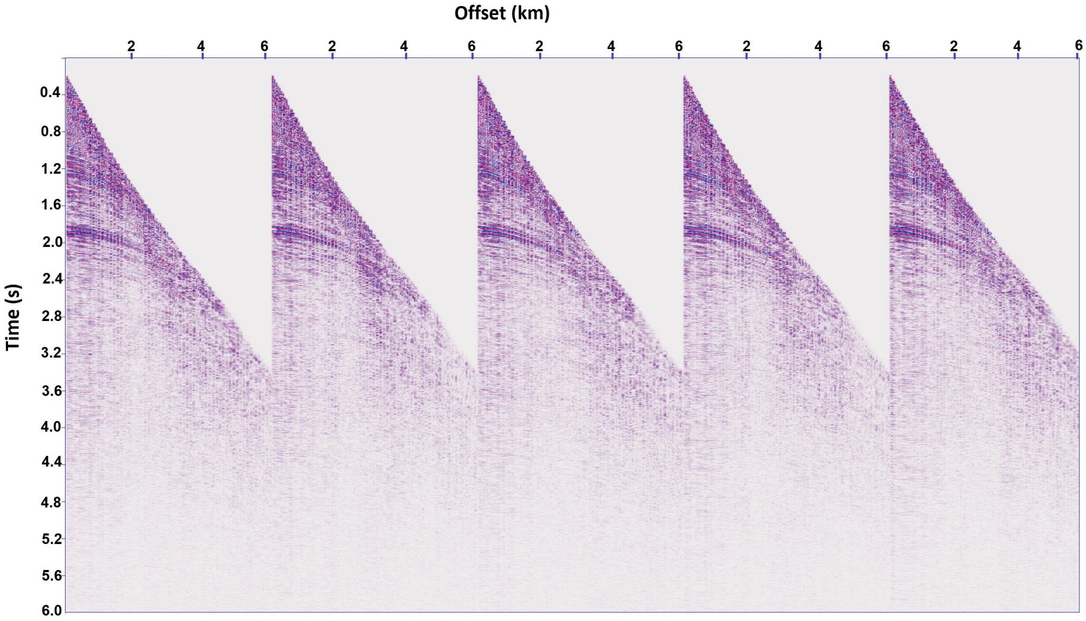

Fig. 8. Several common midpoint gathers of 3D seismic data from the Kara Sea.

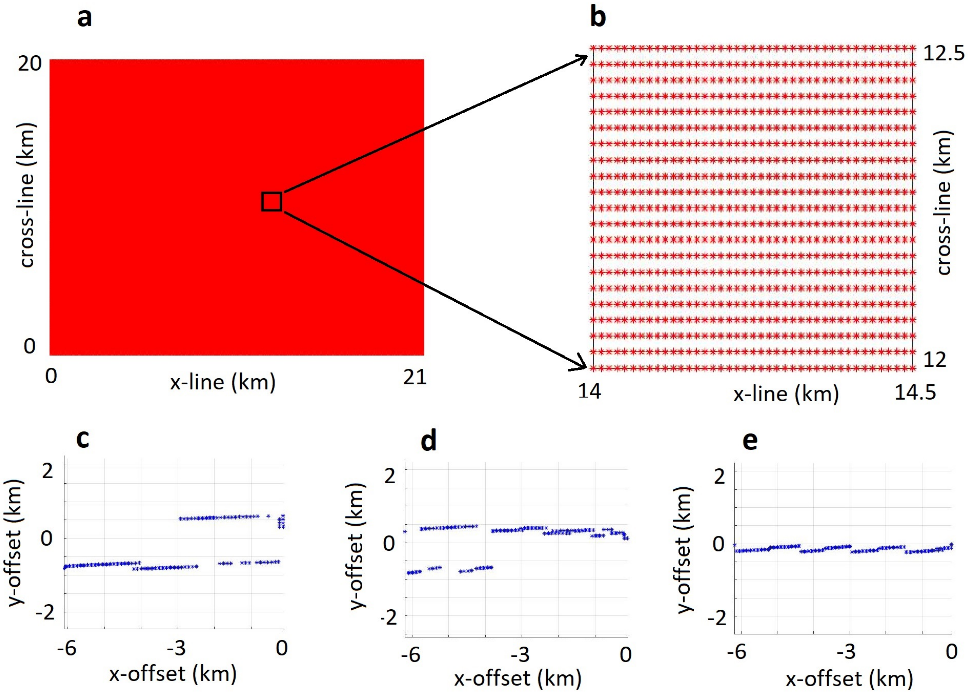

Fig. 9. Midpoints and offsets coordinates after binning of the seismic data from the Kara Sea. a) position of midpoints after binning. b) and their zoom; c) d) e) offset coordinates for three different midpoints.

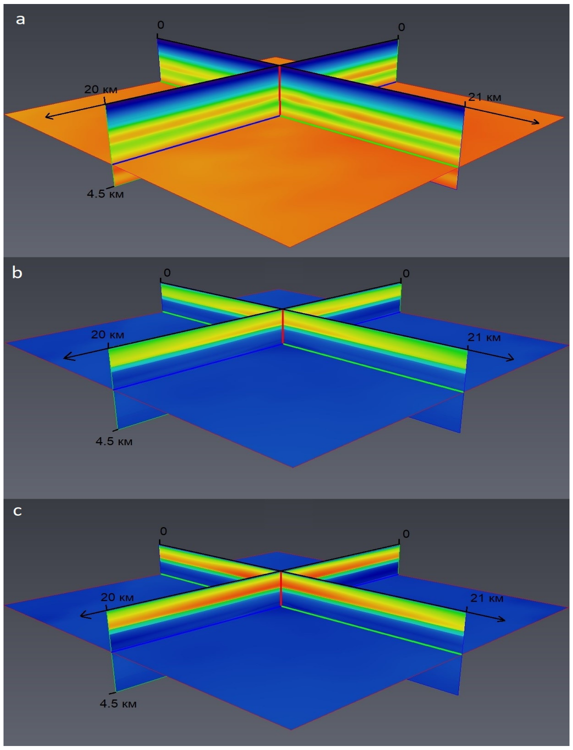

Fig. 10. Migration model got by common image point tomography of 3D seismic data from the Kara Sea. a) P-velocity, anisotropic parameters. b) Thomsen parameter δ . c) Thomsen parameter ε .

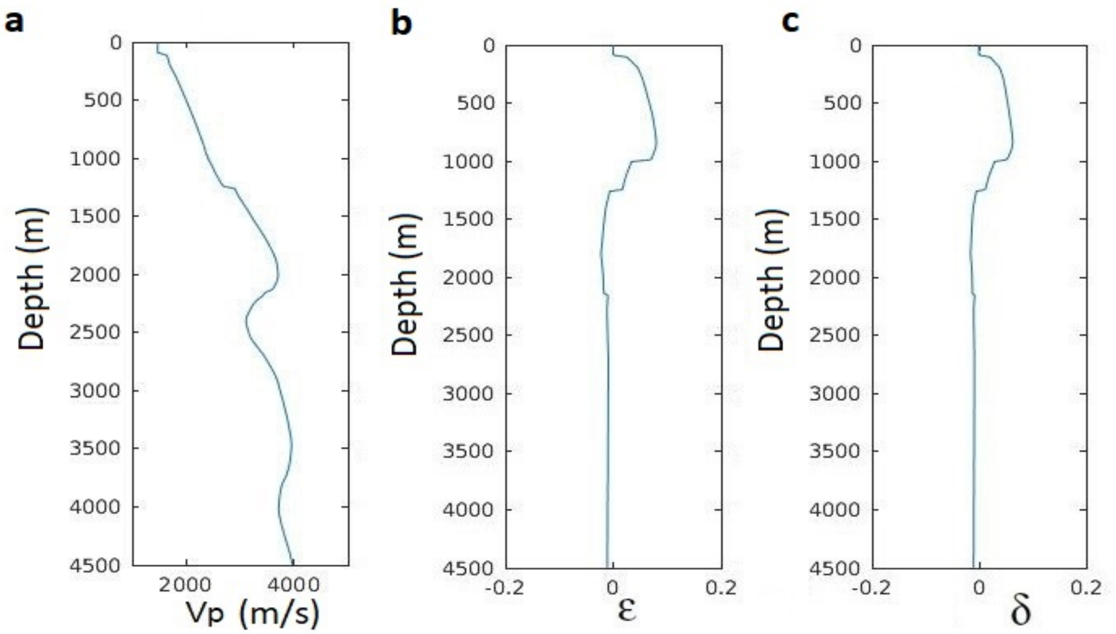

Fig. 11. Depth profiles of the migration model at the point x = 0 y = 0. a) P-velocity, anisotropic parameters. b) Thomsen parameter δ . c) Thomsen parameter ε .

Such an algorithm is not object-oriented and it requires a transformation of recovered true amplitude function from acquisition coordinates to structural angles coordinates. But this way provides a high signal to noise ratio and spatial resolution still and faster realization in terms of beam tracing which is important for big 3D models and big 3D imaging area.

The third algorithm is a slight modification of the second one where:

1) Gaussian beams are traced from the *acquisition points*;
2) Gaussian beams have an equal width at the *acquisition points*;
3) Imaging condition is implemented in terms of the *acquisition coordinates*.

This way provides a good signal to noise ratio still and it gives much faster realization in terms of data summation with beams that is highly important for big 3D seismic data. In comparison with this algorithm (beams have equal width at the acquisition points) the second algorithm (beams have equal width at all imaging points) has better signal to noise ratio at the final image and therefore it can be used, for example, for imaging of rather noisy data or for diffraction imaging where signal to noise ratio plays a crucial role. Otherwise, the third algorithm (beams have an equal width at the acquisition points) provides good enough results that have similar quality with the second one (beams have an equal width at all imaging points).

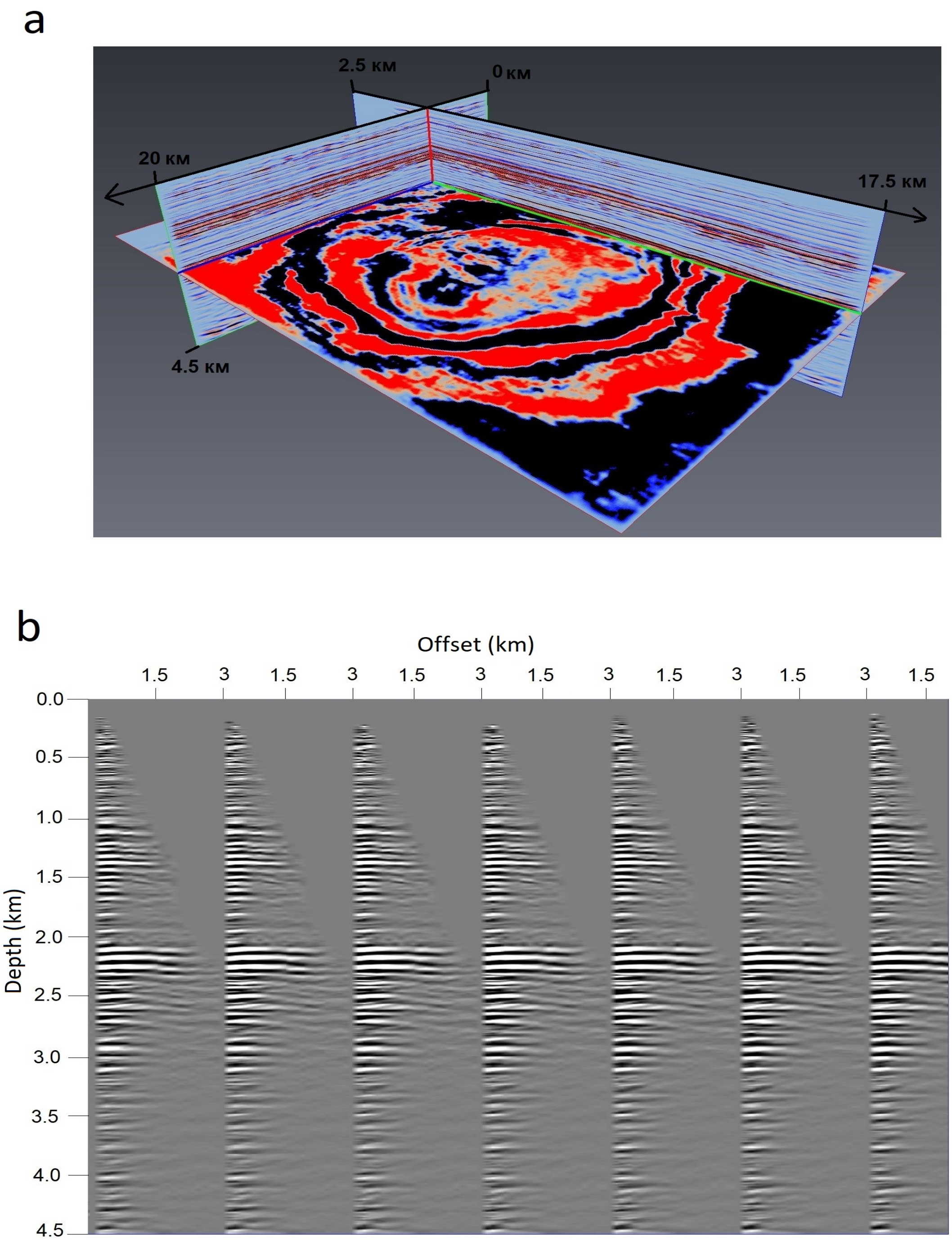

Fig. 12. Results of anisotropic Gaussian beam migration of 3D seismic data from the Kara Sea. a) 3D view of the deep migrated section. b) Common image point seismograms.

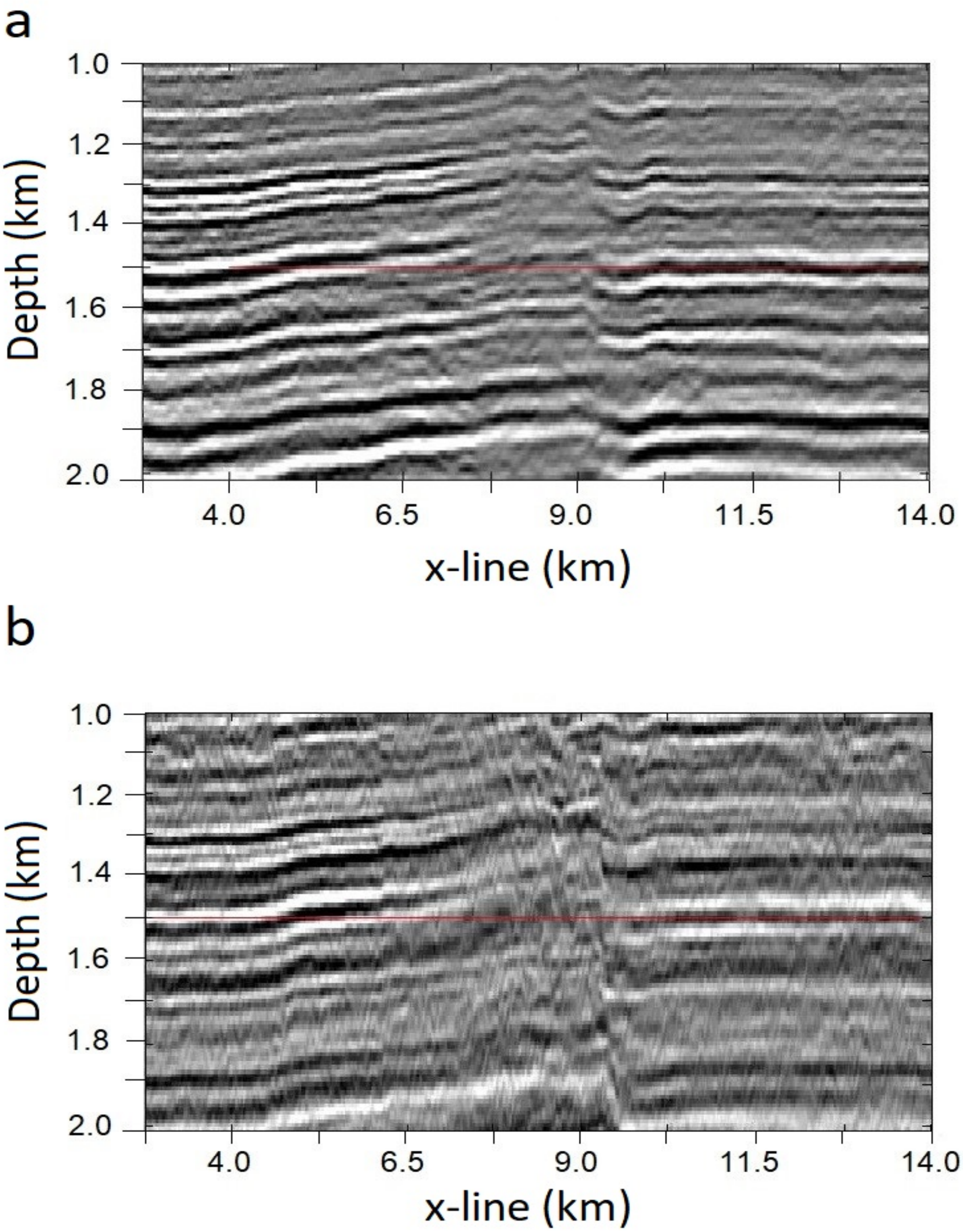

Fig. 13. Depth vertical sections of 3D images got by migration of 3D seismic data from the Kara Sea. a) Result of anisotropic Gaussian beam migration. b) Result of anisotropic Kirchhoff migration.

All the algorithms can be applied to irregular data either in source-receiver or midpoint-offset domains. The migration results for realistic synthetic and real data from the Siberia and from the Kara Sea clear proves the advantages of the developed algorithms. The obtained stacked images and the CIGs are much cleaner and more coherent in comparison with the results of Kirchhoff migration. Consequently, the picking of the events on the common image seismograms should be more robust and hence the application of common image point (CIP) tomography should be more robust and they should make work of CIP tomography more sustainable, therefore the resulting tomographic models should be more correct. It should be noted that, in contrast to Kirchhoff migration, the beam imaging algorithm "chooses" the most coherent events from the data for each image point, therefore, the results in the beam case are less noisy and more coherent than the results of Kirchhoff migration.

ACKNOWLEDGMENTS

The numerical results were obtained through the software belonging to Ltd. INGEOSERVICE. The authors thank Ltd. INGEOSERVICE for the real data and for the permission to publish the results. Also, the research described in this publication was partially supported by RFBR Grant No. 17-05-00001 and by the Russian Academy of Sciences within the scope of project No. 0331-2019-0008.

REFERENCES

Albertin, U., Yingst, D., Kitchenside P. and Tcheverda, V., 2004. True-amplitude beam migration. Expanded Abstr, 74th Ann. Internat. SEG Mtg., Denver: 398-401.

Babich, V.M. and Popov, M.M., 1989. Gaussian beam summation (review). Izvestiya Vysshikh Uchebnykh Zavedenii Radiofizika, 32: 1447-1466 (in Russian, translated in Radiophysics and Quantum Electronics, 32: 1063-1081).

Beylkin, G., 1985. Imaging of discontinuities in the inverse scattering problem by inversion of causal generalized Radon transform. J. Mathemat. Phys., 26: 99-108.

Devaney, A.J., 1984. Geophysical diffraction tomography. IEEE Transact. Geosci. Rem. Sens., 22: 3-13.

Docherty, P., 1991. A brief comparison of some Kirchhoff integral formulas for migration. Geophysics, 56:1164-1169.

Gray, S.H., 2005. Gaussian beam migration of common-shot records. Geophysics, 70(4): S71-S77.

Gray, S. and Bleistein, N., 2009. True amplitude Gaussian-beam migration. Geophysics, 74: S11-S23.

Hill, N.R., 1990. Gaussian beam migration. Geophysics, 55: 1416-1428.

Hill, N.R., 2001. Prestack Gaussian beam depth migration. Geophysics, 66: 1240-1250.

Miller, D., Oristaglio, M. and Beylkin, G., 1987. A new slant on seismic imaging: Migration and integral geometry. Geophysics, 53: 943-964.

Nomofilov, V.E., 1981. Asymptotic solution of a system of equations of second order, which are concentrated in a neighborhood of a ray. Zap. Nauch. Sem. LOMI, 104: 170-179 (in Russian).

Novak, R.L., 2012. A tale of two beams: an elementary overview of Gaussian beams and Bessel beams. Stud. Geophys. Geod., 56: 355.

Popov, M.M., 2002. Ray Theory and Gaussian Beam for Geophysicists. Editoria da Universidade Federal da Bahia, Salvador-Bahia, 172 pp.

Protasov, M.I., 2015. 2D Gaussian beam imaging of multicomponent seismic data in anisotropic media. Geophys. J. Internat., 203: 2021-2031.

Protasov, M.I., Reshetova, G.V. and Tcheverda, V.A., 2016. Fracture detection by Gaussian beam imaging of seismic data and image spectrum analysis. Geophys. Prosp., 64: 68-82.

Protasov, M.I. and Tcheverda, V.A., 2011. True amplitude imaging by inverse generalized Radon transform based on Gaussian beam decomposition of the acoustic Green's function. Geophys. Prosp., 59: 197-209.

Protasov, M.I. and Tcheverda V.A., 2012. True amplitude elastic Gaussian beam imaging of multicomponent walkaway vertical seismic profiling data. Geophys. Prosp., 60: 1030-1042.

Schleicher, J., Tygel, M. and Hubral, P., 1993. 3-D true amplitude finite-offset migration. Geophysics, 58: 1112-1126.

Schleicher, J., Tygel, M. and Hubral, P. 2007. Seismic True-amplitude Imaging. SEG, Tulsa, OK.

SEG/EAGE 3D modeling Salt Model Phase-C, 1996. https://wiki.seg.org/wiki/SEG/EAGE 3D_modeling_Salt_Model_Phase-C_1996.

Vishnevsky, D., Lisitsa, V., Tcheverda, V. and Reshetova G., 2014. Numerical study of the interface errors of finite-difference simulation of seismic waves. Geophysics, 79(4): T219-T232

Zhang, Y., Xu, S., Bleistein, N. and Zhang, G., 2007. True-amplitude, angle-domain, common-image gathers from one-way wave-equation migration. Geophysics, 72(1): S49-S58.

Zhu, T., Gray, S.H. and Wang, D., 2007. Prestack Gaussian-beam depth migration in anisotropic media. Geophysics, 72: S133-S138.